PNAS

www.pnas.org

Supplementary Information for

Evidence for independent brain and neurocranial reorganization during hominin evolution

José Luis Alatorre Warren, Marcia S. Ponce de León, William D. Hopkins, Christoph P. E. Zollikofer.

Corresponding author: José Luis Alatorre Warren
Email: luis.warren@aim.uzh.ch

This PDF file includes:

>   Supplementary text
>   Figs. S1 to S5
>   Tables S1 to S4
>   Captions for movies S1
>   References for SI reference citations

Other supplementary materials for this manuscript include the following:

>   Movies S1

Supplementary Information Text

<u>**Materials and Methods**</u>

Data and image processing and analysis

Except where noted, all image processing and image analysis was performed in MATLAB with extensive use of the toolbox DIPimage (www.diplib.org/dipimage) and the C library DIPlib (www.diplib.org/diplib).

CT and MRI data acquisition

T1- and T2-weighted MRI data of 32 human volunteers were acquired at University Hospital Zurich using a Philips scanner. T1-weighted MRI scans were acquired using the following protocol: TR = 8.3 ms, TE = 3.8 ms, matrix size of 240 × 240, isotropic pixel size of 1 mm, slice spacing of 0.938 mm, and slice thickness of 1.0 mm. T2-weighted MRI scans were acquired using the following protocol: TR = 11000 ms, TE = 120 ms, matrix size of 352 × 258, FOV = 230.00 × 134.00 × 182.95 mm, slice spacing of 5.0 mm, and slice thickness of 4.0 mm.

Anonymized clinical CT/MRI data of 6 human individuals from University Children's Hospital Zurich were acquired using a Philips Brilliance 40 CT scanner and a GE Signa HDxt 1.5-Tesla MRI scanner. The CT data consisted of volumes with isotropic pixels of 0.357–0.432 mm and interslice spacing of 0.625 mm. The MRI data was acquired using the following protocol: TR = 8.4–14.3 ms, TE = 3.4–4.4 ms, matrix size of 512 × 512, isotropic pixel size of 0.430–0.469 mm, slice spacing of 1.0 mm, and slice thickness of 0.625 mm.

Anonymized clinical CT/MRI data of 3 human individuals from University Hospital Leuven were acquired using a Siemens Somatom Definition Flash CT scanner and a Philips Intera 1.5-Tesla MRI scanner. CT data consisted of volumes with isotropic pixels of 0.488–0.583 mm and interslice spacing of 0.700 mm. MRI data was acquired using the following protocol: TR = 9.6 ms, TE = 4.6 ms, matrix size of 256 × 256, isotropic pixel size of 0.977 mm, slice spacing of 1.2 mm, and slice thickness of 1.2 mm.

MRI data of 23 live chimpanzees were acquired at Yerkes National Primate Research Center from sedated individuals, following the protocols described in ref. (1).

Postmortem CT/MRI data of one chimpanzee were acquired at the Primate Research Institute of the University of Kyoto using a Toshiba Asteion CT scanner and a GE Genesis Signa 1.5-Tesla MRI scanner. The CT data consisted of a volume with isotropic pixels of 0.625 mm and interslice spacing of 0.500 mm. The MRI data was acquired using the following protocol: TR = 34.9 ms, TE = 9.4 ms, matrix size of 256 × 256, isotropic pixel size of 1.125 mm, slice spacing of 1.0 mm, and slice thickness of 1.0 mm.

Postmortem CT/MRI data of one gorilla was scanned at the University of Bern using a Philips Brilliance 16P CT scanner and a Philips Panorama HFO 1.0-Tesla MRI scanner. CT consisted of a volume with isotropic pixels of 0.486 mm and interslice spacing of 0.400 mm. Three mutually orthogonal T1-weighted MRI scans were acquired using the following protocol: TR = 400.0 ms, TE = 15.0 ms, matrix size of 720 × 720, isotropic pixel size of 0.236 mm, slice spacing of 4.0 mm, and slice thickness of 3.5 mm. Three mutually orthogonal T2-weighted MRI scans were acquired using the following protocol: TR = 5506.1 ms, TE = 100.0 ms, matrix size of 672 × 672, isotropic pixel size of 0.238 mm, slice spacing of 4.0 mm, and slice thickness of 3.5 mm. Each set of three mutually orthogonal scans were coregistered, resampled, and averaged to obtain a

composite volume with isotropic voxels of 0.5 mm. Both composite volumes (one based on T1-weighted MRI data and the other one on T2-weighted MRI data) were used in subsequent analyses.

Postmortem CT/MRI data of the second gorilla was scanned at the University of Zurich using a Siemens Somatom Definition Flash CT scanner and a Philips Achieva 3.0-Tesla MRI scanner. The CT data consisted of a volume with isotropic pixels of 1.270 mm and interslice spacing of 0.600 mm. Three different MRI scans with different slice acquisition planes were acquired using the following protocols: TR = 8.4 ms, TE = 3.9 ms, matrix size of 384×384, isotropic pixel size of 0.938 mm, slice spacing of 1 mm, and slice thickness of 1 mm; TR = 551.5 ms, TE = 6.4 ms, matrix size of 640×640, isotropic pixel size of 0.5 mm, slice spacing of 3.5 mm, and slice thickness of 2.5 mm; and TR = 2955.8 ms, TE = 60.0 ms, matrix size of 672×672, isotropic pixel size of 0.477 mm, slice spacing of 3.5 mm, and slice thickness of 2.5 mm. These three MRI scans were coregistered, resampled, and fused (maximizing local image contrast) to obtain a composite volume with isotropic voxels of 0.5 mm.

This study makes retrospective use of the datasets; i.e., the original data acquisition was completed before this study was designed.

CT gantry tilt correction

The tools 'gantrycorrect.m' in MATLAB and 'Gantry Tilt correction plugin' in OsiriX (Pixmeo SARL, Bernex, Switzerland) were used for gantry tilt correction in all pediatric CT scans. In all these cases, the correction was performed directly on the raw image data.

CT-based endocast segmentation

Virtual endocasts were created using a fully supervised segmentation procedure in Avizo (v7.1–9.3, Thermo Fisher Scientific-Electron Microscopy Solutions). In brief, the segmentation consisted of a region-growing approach followed by manual delineation and correction on each of the slices of the CT scans. All segmentations were carried out by one of the authors (J.L.A.W.) to avoid interrater variability.

MRI nonuniformity correction

The MRI nonuniformity correction was performed using the N3 nonuniformity correction algorithm (2) as implemented in FireVoxel (NYU Center for Advanced Imaging Innovation and Research, New York, NY) and the 3D Slicer (www.slicer.org) implementation of N4ITKBiasFieldCorrection (3), an improved version of the original N3 algorithm.

Preprocessing of postmortem T2-weigthed MRI scans

In both gorilla datasets of our secondary sample, multiple MRI scans with different slice acquisition planes were available. In these scans, the in-plane resolution was always relatively high (≤1 mm in both spatial dimensions) but the resolution in the third dimension was low (the interslice spacing was typically ≥ 3.0 mm). To obtain a volume with high resolution in all three spatial dimensions, the MRI scans were coregistered and resampled using *elastix* (4) and fused (either by averaging them or by maximizing local image contrast) in MATLAB. In these specimens, landmark data of brain features were sampled on the composite volumes.

MRI-based brain segmentation

In all human T1- and T2-weigthed MRI scans, two different automated brain segmentation algorithms were performed, resulting in two independent segmentations per scan: one using FSL-BET (5) and the other one using FireVoxel (6). In all cases, FSL-BET provided satisfactory results that required no further correction. Therefore, these segmentations were used in further analyses and in the anatomical labeling of all but two brain structures: the *la* and the cerebrum-cerebellum delimitation. For the anatomical labeling of these two structures, the segmentations obtained with FireVoxel were used instead, as this algorithm consistently outperformed FSL-BET at segmenting the ventral regions of the brain, especially those in the vicinity of pons, midbrain, and the inferior portion of the diencephalon.

In all nonhuman T1- and T2-weighted MRI scans, brain segmentation was performed using a set of interactive, region-growing based segmentation tools in Avizo. This procedure was purposely fully supervised to avoid potential biases in automated techniques caused by differences in species and developmental stages, by differences in scanning protocols and/or scanners at different centers, and/or by differences due to living versus postmortem individuals. All segmentations were carried out by one of the authors (J.L.A.W.) to avoid interrater variability.

MRI-based neurocranium segmentation

In all 32 human individuals without CT scans, the neurocranium was segmented from both T1- and T2-weighted MRI data as follows:

(i) First, a first set of rough estimations of the endo- and ectocranial surfaces (inner and outer skull in FSL terminology) was obtained from each pair of T1- and T2-weighted MRI scans using FSL-BET2 with the following parameters: fractional intensity (FA) was set at the default value (FA = 0.5); the parameter center-of-gravity (-c) was roughly set at the center of the trunk of the corpus callosum at the midsagittal plane of each individual (instead of at the default estimation of the image's center of gravity); and finally, the subroutine betsurf (7) was called by including the parameter –A.

Then, a second and a third set of endo- and ectocranial surface estimations were obtained using FA values of 0.4 and 0.3, respectively, and keeping all other parameters the same.

(ii) For each of the 3 sets, a binary segmentation of the actual neurocranium was computed from the mathematical intersection of each pair of endo- and ectocranial surface estimations.

(iii) To ensure that all neurocranial tissue was included in all cases, each of the 3 neurocranium segmentations were dilated (binary morphological operator) with a 3D structuring element of size 1 and a neighborhood of 26 voxels. Here, false positives (non-neurocranial voxels wrongly classified as neurocranium) were preferable than false negatives (neurocranial voxels wrongly classified as non-neurocranium) because false negatives could later be easily removed via thresholding once the MRI intensities were mapped onto the final segmentation.

(iv) A consensus neurocranium NC_{MV} was generated by performing a majority voting scheme from each of the 3 dilated binary segmentations.

(v) The original MRI intensities were mapped onto the NC_{MV}. The resulting volumes were used for the anatomical labeling of neurocranial structures.

In all 23 chimpanzees without CT scans, the neurocranium segmentations were performed on the T1-weighted MRI scans using the interactive, region-growing based segmentation tools in Avizo. Notice that the chimpanzee neurocranium is remarkably quick and uncomplicated to segment in MRI using this approach, and that it would be impractical to proceed in the same way in humans. This is due to the fact that in chimpanzee T1-weighted MRI scans—in contrast to the ones of humans—nearly all dark intensity voxels depicting the neurocranium and/or cerebrospinal fluid (CSF) are exclusively connected to significantly brighter voxels (representing brain or a range of soft tissues).

CT/MRI image registration

All CT/MRI registrations were parametric and intensity-based image registrations, and were performed in elastix (4) and Avizo. In all cases, the gantry-tilt corrected, nonsegmented CT data of each individual was aligned to its associated MRI brain segmentation. All registrations were constrained to exclusively undergo rigid-body transformations (parameter EulerTransform in elastix) and used Normalized Mutual Information (8, 9) (parameter NormalizedMutualInformation in elastix) as a similarity metric. In all cases, the registered volumes preserved their image intensities intact (no image resampling was used) and only their associated spatial (location and orientation) information was modified.

### *Feature extraction, parameterization, and anatomical labeling*

Brain and neurocranial features were manually delineated using the B-spline curve editor in Avizo. In short, a series of points were orderly digitized along each feature following a predefined protocol based on established anatomical references (10-13) and IMAIOS (https://www.imaios.com). These points were then used as control points from where a three-dimensional third-order B-spline curve was approximated for each feature. Initially, each curve consisted of 1000 orderly points or semilandmarks. Then, all semilandmarks were resampled to be approximately equally spaced across features and individuals (interlandmark distance in humans: mean = 1.19 mm, s.d. = 0.08 mm; interlandmark distance in chimpanzees: mean = 0.78 mm, s.d. = 0.08 mm). In this way, a relative weighting was effectively assigned to each feature in function of their length, removing biases stemming from uncorrected dense and sparse sets of points during the geometric morphometrics analyses. All procedures were performed with the software Avizo. In the subsample represented by CT/MRI data, neurocranial features were sampled on the CT datasets. To avoid interrater variability, all delineations were performed by one of the authors (J.L.A.W.).

### *Cross-modality validation of neurocranial feature extraction*

To validate the MRI-based neurocranial delineations, they were also carried out in the set of CT/MRI scans and compared to the ones obtained from CT data, which were used as gold standard. In all instances, the MRI- and CT-based neurocranial delineations coincided noticeably and therefore differences were considered negligible. The CT-based neurocranial delineations of the set of CT/MRI scans were used in subsequent analyses. Non-homologous (taxon-specific) features of interest, such as the *hr* and *ar* in humans and the *fo* and *lu* in great apes, were also delineated and extracted. These features were first analyzed within their own taxon but their averages were later spatially transformed and integrated into the full population consensus. An analogous procedure was performed to integrate modality-specific features, such as the CT-based neurocranial features not included in the reduced set extracted from MRI-only scans.

Morphometric and statistical analysis

In the analyses involving brain and neurocranial features simultaneously, Procrustes superimposition was exclusively based on a subset of brain and endocranial features that exhibit relatively low variability within and between species (see Table S1). In this way, misalignments caused by large differences in ectocranial morphology were avoided. In all other analyses, all the features to be analyzed were used to align the data. All landmark-based geometric morphometrics and statistical analyses were performed in R using the packages Morpho (cran.r-project.org/web/packages/Morpho) and geomorph (cran.r-project.org/web/packages/geomorph) extensively.
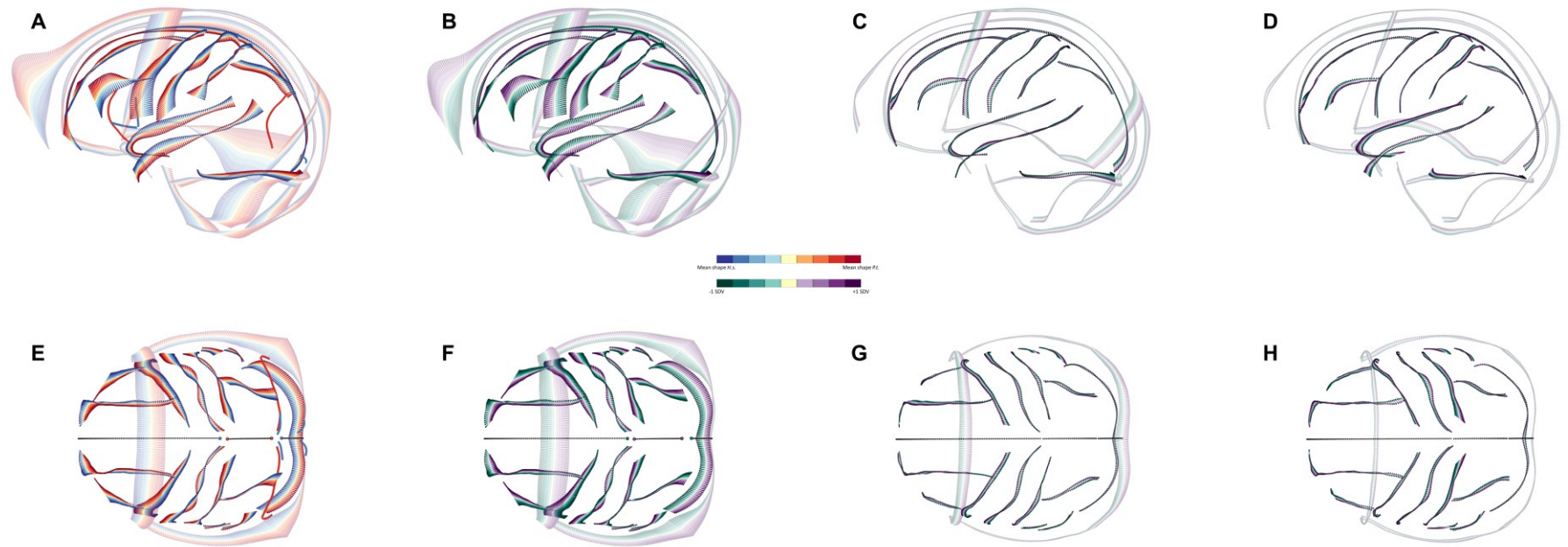
Fig. S1. Differences between human and chimpanzee neurocranium+brain configurations. Differences in physical space between the human (blue) and chimpanzee (red) mean shapes (*A, E*), and between the shapes associated with ±1 standard deviations along PC1 (*B, F*), PC2 (*C, G*), and PC3 (*D, H*) from the principal component analysis of neurocranium+brain shape variation in humans and chimpanzees.
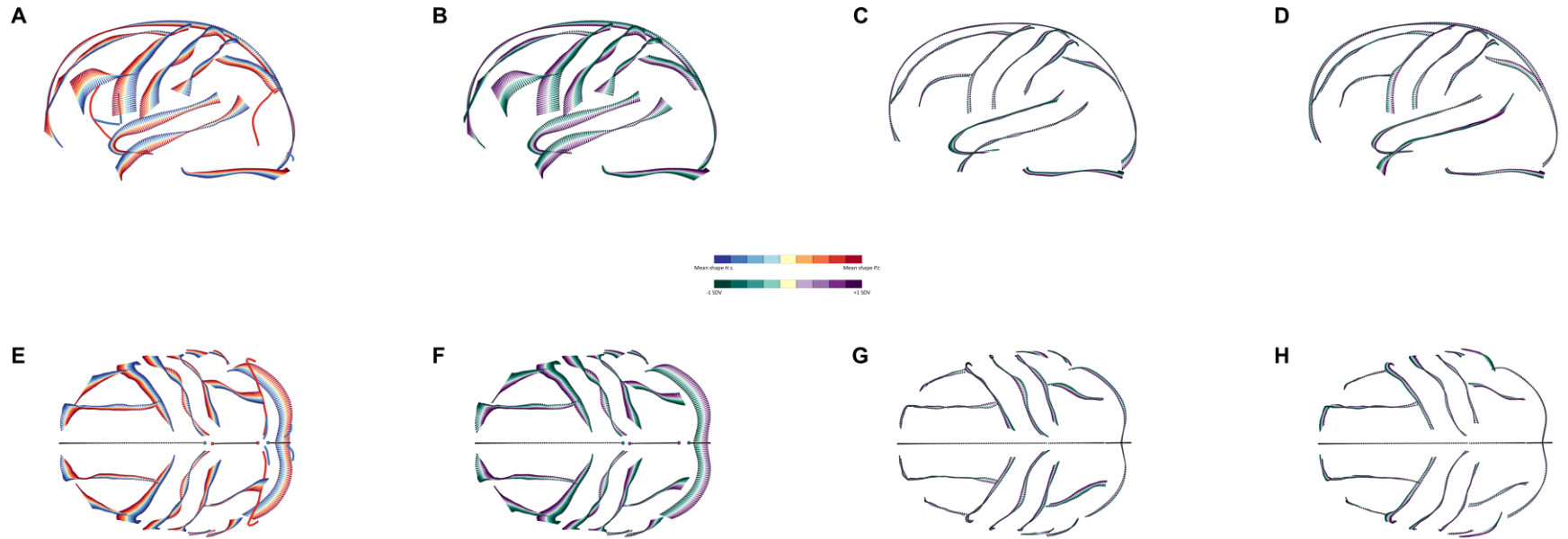
Fig. S2. Differences between human and chimpanzee brain configurations. Differences in physical space between the human (blue) and chimpanzee (red) mean shapes (*A*, *E*), and between shapes associated with ±1 standard deviations along PC1 (*B*, *F*), PC2 (*C*, *G*), and PC3 (*D*, *H*) from the principal component analysis of brain shape variation in humans and chimpanzees.
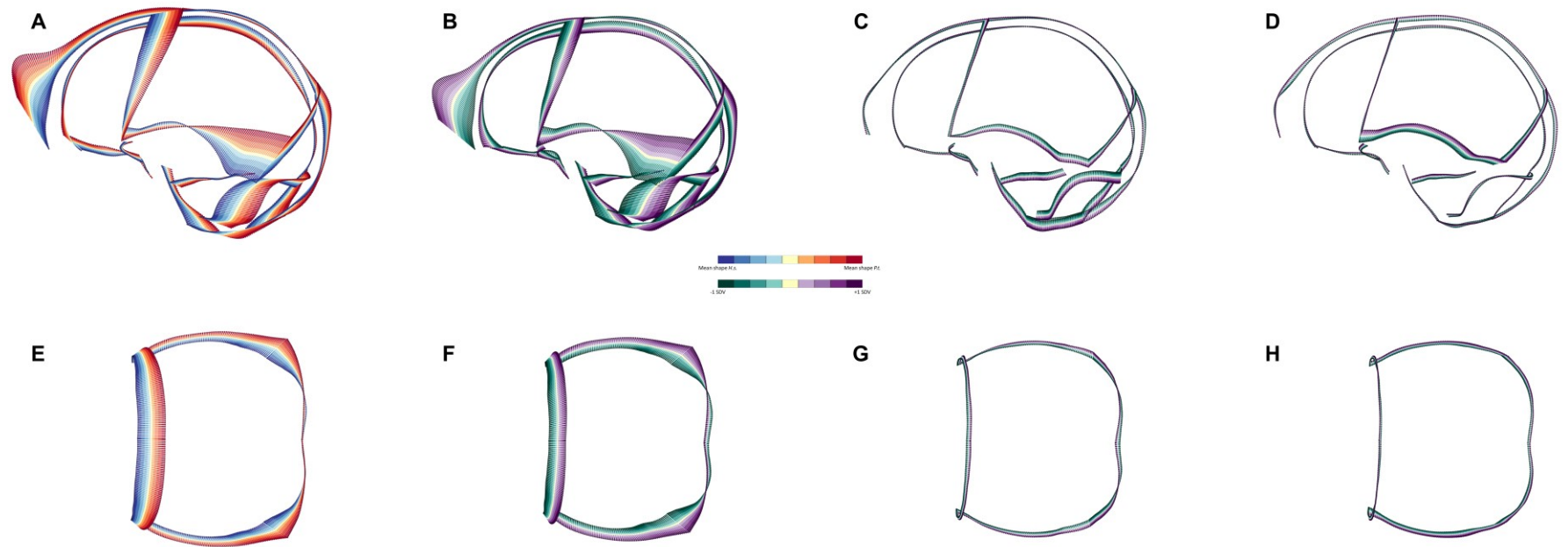
Fig. S3. Differences between human and chimpanzee neurocranium configurations. Differences in physical space between the human (blue) and chimpanzee (red) mean shapes (*A, E*), and between the shapes associated with ±1 standard deviations along PC1 (*B, F*), PC2 (*C, G*), and PC3 (*D, H*) from the principal component analysis of neurocranial shape variation in humans and chimpanzees.

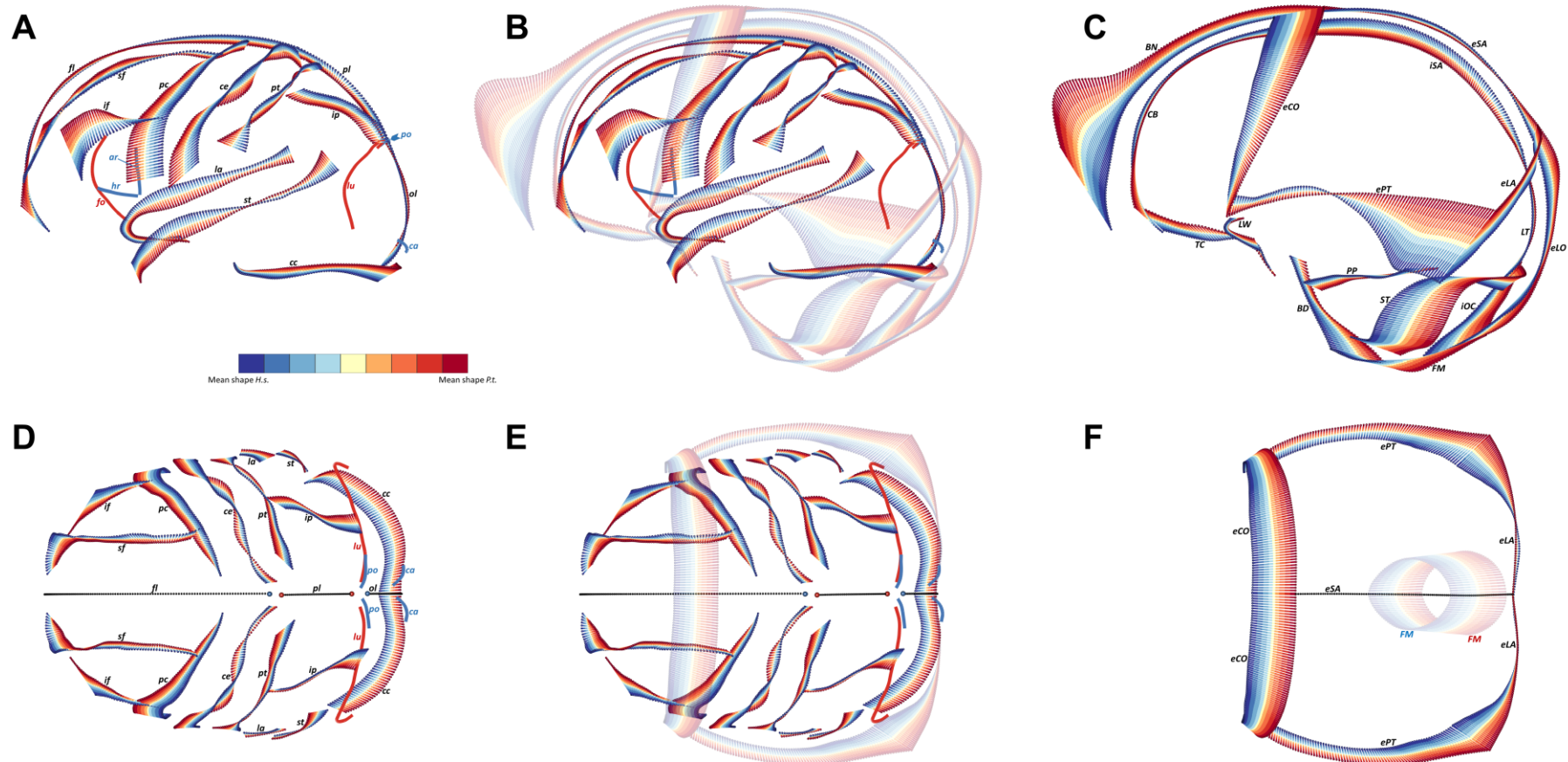**Fig. S4.** Differences between human (blue) and chimpanzee (red) mean configurations for brain (*A, D*), neurocranium (*C, F*) and neurocranium+brain (*B, E*).
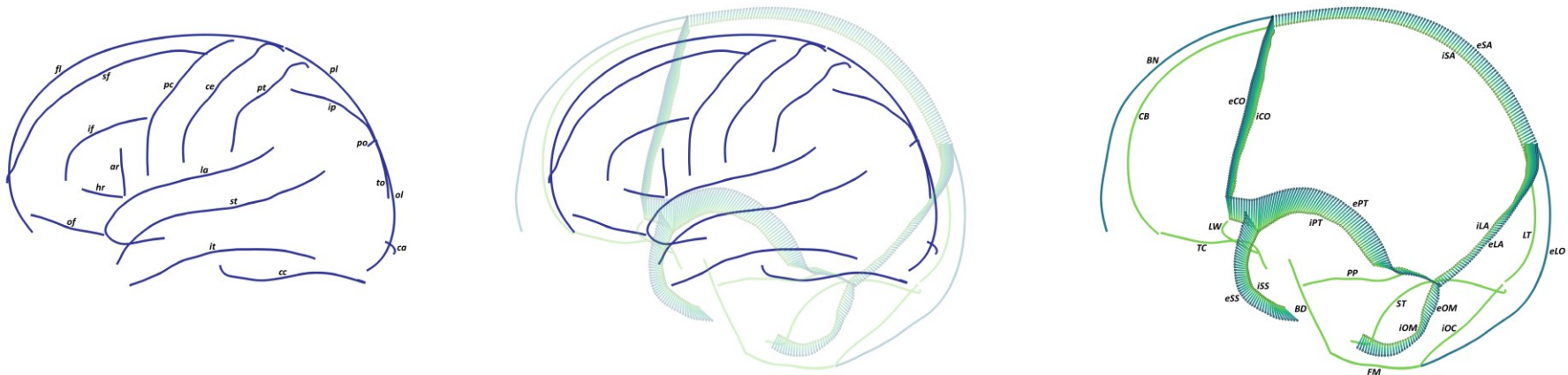
Fig. S5. Visualization of the topographical relationships between brain (dark blue), endocranial (light green), and ectocranial (dark green) features in humans. Human brain (left), neurocranium (right), and neurocranium+brain (center). Lines connecting points describe the distance between endo- and ectocranial sutures. The mean shapes of *iCO*, *iLA*, *iPT*, *iOM*, *iSS*, *eOM*, and *eSS* shown here were computed from the subsample of 9 human CT/MRI datasets; the mean shapes of all other features were computed over the full sample of 41 humans.

Table S1

Brain and neurocranial features.

				Parietal	GPA	Humans MRI	Humans CT/MRI	Great apes MRI	Great apes CT/MRI
Set 1 – Features sampled in all 41 humans, 24 chimpanzees, and 2 gorillas									
1,2	Brain	*cc*	Cerebrum-cerebellum delimitation		√	√	√	√	√
3	Brain	*fl*	Frontal lobe segment of the medial longitudinal fissure		√	√	√	√	√
4	Brain	*ol*	Occipital lobe segment of the medial longitudinal fissure		√	√	√	√	√
5	Brain	*pl*	Parietal lobe segment of the medial longitudinal fissure		√	√	√	√	√
6,7	Brain	*ce*	Central sulcus	B	√	√	√	√	√
8,9	Brain	*if*	Inferior frontal sulcus			√	√	√	√
10,11	Brain	*sf*	Superior frontal sulcus			√	√	√	√
12,13	Brain	*ip*	Intraparietal sulcus	B	√	√	√	√	√
14,15	Brain	*la*	Lateral sulcus	B	√	√	√	√	√
16,17	Brain	*pt*	Postcentral sulcus	B	√	√	√	√	√
18,19	Brain	*pc*	Precentral sulcus	B	√	√	√	√	√
20,21	Brain	*st*	Superior temporal sulcus	B		√	√	√	√
22,23	Internal neurocranium	*LW*	Posterior border of the lesser wing of the sphenoid bone		√	√	√	√	√
24	Internal neurocranium	*BD*	Curve from basion to dorsum sellae			√	√	√	√
25	Internal neurocranium	*iOC*	Internal occipital crest			√	√	√	√
26	Internal neurocranium	*FM*	Foramen magnum			√	√	√	√
27,28	Internal neurocranium	*PP*	Superior margin of the petrous part of the temporal bone			√	√	√	√
29	Internal neurocranium	*CB*	Curve from foramen caecum to bregma			√	√	√	√
30	Internal neurocranium	*LT*	Curve from lambda to the transverse sinus at the midline			√	√	√	√
31	Internal neurocranium	*iSA*	Sagittal suture	N		√	√	√	√
32	Internal neurocranium	*TC*	Curve from sella turcica to foramen caecum		√	√	√	√	√
33,34	Internal neurocranium	*ST*	Sigmoid and transverse sinuses			√	√	√	√
35,36	External neurocranium	*ePT*	Parietotemporal suture (curve from asterion to pterion)	N		√	√	√	√
37	External neurocranium	*BN*	Curve from bregma to nasion			√	√	√	√
38	External neurocranium	*eLO*	Curve from lambda to opisthion			√	√	√	√
39,40	External neurocranium	*eCO*	Coronal suture	N		√	√	√	√
41,42	External neurocranium	*eLA*	Lambdoid suture	N		√	√	√	√
43	External neurocranium	*eSA*	Sagittal suture	N		√	√	√	√
Set 2 – Additional features sampled in all 41 human individuals									
44,45	Brain	*hr*	Horizontal ramus of the lateral sulcus			√	√		
46,47	Brain	*ar*	Ascending ramus of the lateral sulcus			√	√		
48,49	Brain	*ca*	Dorsolateral segment of the calcarine sulcus			√	√		
50,51	Brain	*to*	Transverse occipital sulcus			√	√		
52,53	Brain	*of*	Olfactory sulcus			√	√		
54,55	Brain	*po*	Dorsolateral segment of the parietooccipital sulcus			√	√		
56,57	Brain	*it*	Inferior temporal sulcus			√	√		
Set 3 – Additional features sampled in all 24 chimpanzees and 2 gorillas									
58,59	Brain	*fo*	Fronto-orbital sulcus					√	√
60,61	Brain	*lu*	Lunate sulcus					√	√
Set 4 – Additional features sampled in all 9 human, 1 chimpanzee, and 2 gorilla CT/MRI datasets									
62,63	Internal neurocranium	*HC*	Hypoglossal canal				√		√
64,65	Internal neurocranium	*SO*	Superior orbital fissure				√		√
66,67	Internal neurocranium	*JF*	Jugular foramen				√		√
68,69	Internal neurocranium	*FL*	Foramen lacerum				√		√
70,71	Internal neurocranium	*OF*	Optic foramen				√		√
72,73	Internal neurocranium	*FO*	Foramen ovale				√		√
74,75	Internal neurocranium	*iCO*	Coronal suture				√		√
76,77	Internal neurocranium	*iLA*	Lambdoid suture				√		√
78,79	Internal neurocranium	*iOM*	Occipitomastoid suture				√		√
80,81	Internal neurocranium	*iSS*	Sphenosquamosal suture				√		√
82,83	External neurocranium	*eOM*	Occipitomastoid suture				√		√
84,85	External neurocranium	*SF*	Sphenofrontal suture				√		√
86,87	External neurocranium	*eSS*	Sphenosquamosal suture				√		√
Set 5 – Additional features sampled in all 9 human CT/MRI datasets									
88,89	Internal neurocranium	*FS*	Foramen spinosum				√		
90,91	Internal neurocranium	*iPM*	Parietomastoid suture				√		
92,93	Internal neurocranium	*iSP*	Sphenoparietal suture				√		
94,95	Internal neurocranium	*iSQ*	Squamous suture				√		
96,97	External neurocranium	*ePM*	Parietomastoid suture				√		
98,99	External neurocranium	*eSP*	Sphenoparietal suture				√		
100,101	External neurocranium	*eSQ*	Squamous suture				√		
Set 6 – Additional features sampled in 1 chimpanzee and 2 gorilla CT/MRI datasets									
102,103	Internal neurocranium	*iPT*	Parietotemporal suture (curve from asterion to pterion)						√

In humans, *iPT* is comprised by *iSP*, *iSQ*, and *iPM*, and, similarly, *ePT* is comprised by *eSP*, *eSQ*, and *ePM*. Where appropriate (e.g., between-taxon analyses, analyses of integration and modularity) *iPT* and *ePT* were used in humans.

Table S2

Within-species size-related effects on brain (B), neurocranial (N), and neurocranial+brain (NB) shape variation.

		H.s. (N = 41)			P.t. (N = 24)		
		NB	B	N	NB	B	N
		3258 points	1573 points	1685 points	3258 points	1573 points	1685 points
dense	R^2	0.028	0.027	0.023	0.033	0.032	0.033
dense	*p*-value	0.258	0.341	0.559	0.848	0.776	0.780

p-values represent the proportion of instances with higher R^2 in 10,000 random models

Table S3

Multivariate multiple regression (MMR), partial least squares (PLS) and covariance ratios (CR) between brain (B) and neurocranial (N) features.

		Hemispheres	B semilandmarks	N semilandmarks	Spatial correlation (MMR) R^2 Pooled $N=65$	R^2 H.s. $N=41$	R^2 P.t. $N=24$	Morphological integration (PLS) RV Pooled $N=65$	RV H.s. $N=41$	RV P.t. $N=24$	Morphological modularity (CR) CR Pooled $N=65$	CR H.s. $N=41$	CR P.t. $N=24$
Dense	N vs B [all features]	Both	1573	1685	0.632	0.475	0.678						
Dense	N vs B [all features]	Right	900	1228	0.634	0.467	0.708						
Dense	N vs B [all features]	Left	900	1228	0.604	0.462	0.685						
Dense	N vs B [parietal region]	Both	770	746	0.483	0.373	0.499						
Dense	N vs B [parietal region]	Right	405	475	0.469	0.368	0.551						
Dense	N vs B [parietal region]	Left	405	475	0.457	0.373	0.469						
Sparse	N vs B [all features]	Both	200	211	0.628	0.463	0.678	0.959	0.836	0.851	0.936	0.718	0.778
Sparse	N vs B [all features]	Right	144	155	0.638	0.459	0.700	0.959	0.814	0.851	0.935	0.678	0.782
Sparse	N vs B [all features]	Left	114	155	0.611	0.459	0.693	0.961	0.852	0.814	0.938	0.684	0.754
Sparse	N vs B [parietal region]	Both	99	91	0.485	0.362	0.498	0.937	0.680	0.833	0.869	0.564	0.626
Sparse	N vs B [parietal region]	Right	52	58	0.469	0.377	0.541	0.922	0.636	0.680	0.845	0.505	0.606
Sparse	N vs B [parietal region]	Left	52	58	0.449	0.356	0.486	0.931	0.662	0.787	0.858	0.507	0.584
Extremes	N vs B [all features]	Both	42	44	0.600	0.426	0.665	0.956	0.848	0.856	0.964	0.787	0.835
Extremes	N vs B [all features]	Right	24	32	0.605	0.417	0.637	0.953	0.820	0.848	0.982	0.790	0.843
Extremes	N vs B [all features]	Left	24	32	0.581	0.411	0.689	0.953	0.846	0.837	0.981	0.760	0.865
Extremes	N vs B [parietal region]	Both	22	16	0.447	0.315	0.498	0.921	0.672	0.877	0.928	0.620	0.731
Extremes	N vs B [parietal region]	Right	12	10	0.433	0.354	0.539	0.895	0.624	0.727	0.953	0.621	0.737
Extremes	N vs B [parietal region]	Left	12	10	0.408	0.284	0.468	0.916	0.638	0.822	0.968	0.590	0.756

		Hemispheres	B semilandmarks	N semilandmarks	Spatial correlation (MMR) p-value Pooled $N=65$	p-value H.s. $N=41$	p-value P.t. $N=24$	Morphological integration (PLS) p-value Pooled $N=65$	p-value H.s. $N=41$	p-value P.t. $N=24$	Morphological modularity (CR) p-value Pooled $N=65$	p-value H.s. $N=41$	p-value P.t. $N=24$
Dense	N vs B [all features]	Both	1573	1685	0.001	0.001	0.001						
Dense	N vs B [all features]	Right	900	1228	0.001	0.001	0.001						
Dense	N vs B [all features]	Left	900	1228	0.001	0.001	0.001						
Dense	N vs B [parietal region]	Both	770	746	0.001	0.002	0.123						
Dense	N vs B [parietal region]	Right	405	475	0.001	0.003	0.009						
Dense	N vs B [parietal region]	Left	405	475	0.001	0.003	0.248						
Sparse	N vs B [all features]	Both	200	211	0.001	0.001	0.001	0.001	0.002	0.006	0.001	0.001	0.001
Sparse	N vs B [all features]	Right	114	155	0.001	0.001	0.001	0.001	0.001	0.004	0.001	0.001	0.001
Sparse	N vs B [all features]	Left	114	155	0.001	0.001	0.001	0.001	0.001	0.023	0.001	0.001	0.001
Sparse	N vs B [parietal region]	Both	99	91	0.001	0.003	0.122	0.001	0.073	0.020	0.001	0.001	0.001
Sparse	N vs B [parietal region]	Right	52	58	0.001	0.003	0.016	0.001	0.058	0.485	0.001	0.001	0.001
Sparse	N vs B [parietal region]	Left	52	58	0.001	0.005	0.156	0.001	0.044	0.030	0.001	0.001	0.001
Extremes	N vs B [all features]	Both	42	44	0.001	0.001	0.001	0.001	0.007	0.004	0.001	0.001	0.001
Extremes	N vs B [all features]	Right	24	32	0.001	0.001	0.001	0.001	0.002	0.002	0.003	0.001	0.006
Extremes	N vs B [all features]	Left	24	32	0.001	0.001	0.001	0.001	0.001	0.018	0.004	0.001	0.013
Extremes	N vs B [parietal region]	Both	22	16	0.001	0.021	0.099	0.001	0.305	0.001	0.004	0.001	0.004
Extremes	N vs B [parietal region]	Right	12	10	0.001	0.004	0.011	0.001	0.225	0.361	0.034	0.001	0.057
Extremes	N vs B [parietal region]	Left	12	10	0.001	0.140	0.235	0.001	0.193	0.007	0.043	0.001	0.053

MMR was computed between the first 10 PCs of the PCA of neurocranial shape variation and the first 10 PCs of the PCA of brain shape variation. The RV coefficient ranges from 0 to 1, with higher values indicating higher covariation between modules. The CR coefficient ranges from 0 to positive values, with higher values indicating higher proportion of covariation between modules relative to the total amount of covariation within modules. The CR coefficient has an expected value of 1 for random sets of variables; values between 0 and 1 are thus expected in modular structures. The subset of 6 brain and 5 neurocranial features that comprised the analyses of the parietal region are listed in Table S1. p-values represent the proportion of instances with higher R^2, and lower RV and CR observed in 1000 random models.

Table S4
Specimens.

Name	Species	Sex	Age	Modality	Type	Source
kispi001	*Homo sapiens*	m	7	CT/MRI	*In vivo*	University Children's Hospital Zurich, Switzerland
kispi002	*Homo sapiens*	f	4	CT/MRI	*In vivo*	University Children's Hospital Zurich, Switzerland
kispi003	*Homo sapiens*	m	8	CT/MRI	*In vivo*	University Children's Hospital Zurich, Switzerland
kispi004	*Homo sapiens*	m	9	CT/MRI	*In vivo*	University Children's Hospital Zurich, Switzerland
kispi005	*Homo sapiens*	f	13	CT/MRI	*In vivo*	University Children's Hospital Zurich, Switzerland
kispi006	*Homo sapiens*	f	15	CT/MRI	*In vivo*	University Children's Hospital Zurich, Switzerland
leuven001	*Homo sapiens*	f	49	CT/MRI	*In vivo*	University Hospitals Leuven, Belgium
leuven002	*Homo sapiens*	m	74	CT/MRI	*In vivo*	University Hospitals Leuven, Belgium
leuven005	*Homo sapiens*	f	19	CT/MRI	*In vivo*	University Hospitals Leuven, Belgium
K001	*Homo sapiens*	f	25	MRI	*In vivo*	University Hospital Zurich, Switzerland
K002	*Homo sapiens*	f	31	MRI	*In vivo*	University Hospital Zurich, Switzerland
K003	*Homo sapiens*	f	> 18	MRI	*In vivo*	University Hospital Zurich, Switzerland
K004	*Homo sapiens*	f	29	MRI	*In vivo*	University Hospital Zurich, Switzerland
K009	*Homo sapiens*	m	22	MRI	*In vivo*	University Hospital Zurich, Switzerland
K010	*Homo sapiens*	m	36	MRI	*In vivo*	University Hospital Zurich, Switzerland
K011	*Homo sapiens*	f	19	MRI	*In vivo*	University Hospital Zurich, Switzerland
K015	*Homo sapiens*	m	26	MRI	*In vivo*	University Hospital Zurich, Switzerland
K016	*Homo sapiens*	f	18	MRI	*In vivo*	University Hospital Zurich, Switzerland
K017	*Homo sapiens*	f	25	MRI	*In vivo*	University Hospital Zurich, Switzerland
K018	*Homo sapiens*	f	35	MRI	*In vivo*	University Hospital Zurich, Switzerland
K019	*Homo sapiens*	f	29	MRI	*In vivo*	University Hospital Zurich, Switzerland
K020	*Homo sapiens*	f	24	MRI	*In vivo*	University Hospital Zurich, Switzerland
K021	*Homo sapiens*	m	20	MRI	*In vivo*	University Hospital Zurich, Switzerland
K022	*Homo sapiens*	f	20	MRI	*In vivo*	University Hospital Zurich, Switzerland
K023	*Homo sapiens*	m	31	MRI	*In vivo*	University Hospital Zurich, Switzerland
K024	*Homo sapiens*	f	23	MRI	*In vivo*	University Hospital Zurich, Switzerland
K025	*Homo sapiens*	f	23	MRI	*In vivo*	University Hospital Zurich, Switzerland
K026	*Homo sapiens*	m	24	MRI	*In vivo*	University Hospital Zurich, Switzerland
K027	*Homo sapiens*	m	23	MRI	*In vivo*	University Hospital Zurich, Switzerland
K029	*Homo sapiens*	f	22	MRI	*In vivo*	University Hospital Zurich, Switzerland
K030	*Homo sapiens*	m	31	MRI	*In vivo*	University Hospital Zurich, Switzerland
K031	*Homo sapiens*	f	26	MRI	*In vivo*	University Hospital Zurich, Switzerland
K033	*Homo sapiens*	f	22	MRI	*In vivo*	University Hospital Zurich, Switzerland
K034	*Homo sapiens*	f	28	MRI	*In vivo*	University Hospital Zurich, Switzerland
K035	*Homo sapiens*	f	23	MRI	*In vivo*	University Hospital Zurich, Switzerland
K036	*Homo sapiens*	m	25	MRI	*In vivo*	University Hospital Zurich, Switzerland
K037	*Homo sapiens*	m	33	MRI	*In vivo*	University Hospital Zurich, Switzerland
K038	*Homo sapiens*	m	24	MRI	*In vivo*	University Hospital Zurich, Switzerland
K039	*Homo sapiens*	m	21	MRI	*In vivo*	University Hospital Zurich, Switzerland
K040	*Homo sapiens*	m	24	MRI	*In vivo*	University Hospital Zurich, Switzerland
KJ001	*Homo sapiens*	f	18	MRI	*In vivo*	University Hospital Zurich, Switzerland
pan001	*Pan troglodytes*	m	22	CT/MRI	Post mortem	Primate Research Institute of the Kyoto University, Japan
abby	*Pan troglodytes*	f	13	MRI	*In vivo*	Yerkes National Primate Research Center at Emory University, USA
amanda	*Pan troglodytes*	f	10	MRI	*In vivo*	Yerkes National Primate Research Center at Emory University, USA
angie	*Pan troglodytes*	f	N/A	MRI	*In vivo*	Yerkes National Primate Research Center at Emory University, USA
barney	*Pan troglodytes*	m	15	MRI	*In vivo*	Yerkes National Primate Research Center at Emory University, USA
bart	*Pan troglodytes*	m	N/A	MRI	*In vivo*	Yerkes National Primate Research Center at Emory University, USA
billy	*Pan troglodytes*	m	N/A	MRI	*In vivo*	Yerkes National Primate Research Center at Emory University, USA
bo	*Pan troglodytes*	f	35	MRI	*In vivo*	Yerkes National Primate Research Center at Emory University, USA
brandy	*Pan troglodytes*	f	16	MRI	*In vivo*	Yerkes National Primate Research Center at Emory University, USA
brodie	*Pan troglodytes*	f	24	MRI	*In vivo*	Yerkes National Primate Research Center at Emory University, USA
callie	*Pan troglodytes*	f	15	MRI	*In vivo*	Yerkes National Primate Research Center at Emory University, USA
carl	*Pan troglodytes*	m	15	MRI	*In vivo*	Yerkes National Primate Research Center at Emory University, USA
cissie	*Pan troglodytes*	f	N/A	MRI	*In vivo*	Yerkes National Primate Research Center at Emory University, USA
cybil	*Pan troglodytes*	f	N/A	MRI	*In vivo*	Yerkes National Primate Research Center at Emory University, USA
elwood	*Pan troglodytes*	m	13	MRI	*In vivo*	Yerkes National Primate Research Center at Emory University, USA
evelyne	*Pan troglodytes*	f	15	MRI	*In vivo*	Yerkes National Primate Research Center at Emory University, USA
jake	*Pan troglodytes*	m	N/A	MRI	*In vivo*	Yerkes National Primate Research Center at Emory University, USA
jcarter	*Pan troglodytes*	m	24	MRI	*In vivo*	Yerkes National Primate Research Center at Emory University, USA
jolson	*Pan troglodytes*	m	14	MRI	*In vivo*	Yerkes National Primate Research Center at Emory University, USA
joseph	*Pan troglodytes*	m	27	MRI	*In vivo*	Yerkes National Primate Research Center at Emory University, USA
laz	*Pan troglodytes*	m	20	MRI	*In vivo*	Yerkes National Primate Research Center at Emory University, USA
lulu	*Pan troglodytes*	f	44	MRI	*In vivo*	Yerkes National Primate Research Center at Emory University, USA
lyk	*Pan troglodytes*	m	44	MRI	*In vivo*	Yerkes National Primate Research Center at Emory University, USA
merv	*Pan troglodytes*	m	25	MRI	*In vivo*	Yerkes National Primate Research Center at Emory University, USA
enea	*Gorilla gorilla*	f	8	CT/MRI	Post mortem	Swiss Zoos
nache	*Gorilla gorilla*	f	32	CT/MRI	Post mortem	Swiss Zoos

Movie S1
Visualization of differences between human (blue) and chimpanzee (red) mean configurations of neurocranial and brain features.

References

1. Sherwood CC, Gordon A, Allen J, Phillips K, Erwin J, Hof P, Hopkins W (2011) Aging of the cerebral cortex differs between humans and chimpanzees. *Proc Natl Acad Sci* 108(32).
2. Sled JG, Zijdenbos AP, Evans AC (1998) A nonparametric method for automatic correction of intensity nonuniformity in MRI data. *IEEE Trans Med Imaging* 17(1):87–97.
3. Tustison NJ, Avants B, Cook P, Zheng Y, Egan A, Yushkevich P, Gee J (2010) N4ITK: Improved N3 Bias Correction. *IEEE Trans Med Imaging* 29(6):1310–1320.
4. Klein S, Staring M, Murphy K, Viergever MA, Pluim JPW (2010) elastix: A Toolbox for Intensity-Based Medical Image Registration. *IEEE Trans Med Imaging* 29(1):196–205.
5. Smith SM (2002) Fast Robust Automated Brain Extraction. *Hum Brain Mapp*, 17(3), 143-155.
6. Mikheev A, Nevsky G, Govindan S, Grossman R, Rusinek H (2008) Fully automatic segmentation of the brain from T1-weighted MRI using Bridge Burner algorithm. J *Magn Reson Imaging* 27(6):1235–1241.
7. Jenkinson M, Pechaud M, Smith S (2002) BET2 - MR-Based Estimation of Brain, Skull and Scalp Surfaces.
8. Maes F, Collignon A, Vandermeulen D, Marchal G, Suetens P (1997) Multimodality image registration by maximization of mutual information. *IEEE Trans Med Imaging* 16(2):187–198.
9. Studholme C, Hill DLG, Hawkes DJ (1999) An overlap invariant entropy measure of 3D medical image alignment. *Pattern Recognit* 32(1):71–86.
10. Connolly CJ (1950) *External Morphology of the Primate Brain.* (CC Thomas, Springfield, IL)
11. Bogart SL, Mangin J, Schapiro S, Reamer L, Bennett A, Pierre P, Hopkins W (2012) Cortical sulci asymmetries in chimpanzees and macaques: A new look at an old idea. *Neuroimage* 61(3):533–541.
12. Keller SS, Deppe M, Herbin M, Gilissen E (2012) Variability and asymmetry of the sulcal contours defining Broca's area homologue in the chimpanzee brain. *J Comp Neurol* 520(6):1165–1180.
13. White TD, Black MT, Folkens PA (2011) *Human Osteology* (Third Edition). Academic press.